A virtual calibration strategy and its validation for large-scale models of multi-sheet self-piercing rivet connections

Victor André, Miguel Costas*, Magnus Langseth, David Morin

Structural Impact Laboratory (SIMLab) and Centre for Advanced Structural Analysis (CASA), Department of Structural Engineering, Norwegian University of Science and Technology (NTNU), NO-7491 Trondheim, Norway

Abstract

This paper presents a strategy for the virtual calibration of a large-scale model representing a self-piercing rivet (SPR) connection. The connection is formed between a stack of three AA6016-T4 aluminium sheets and one SPR. The calibration process involves material characterisation, a detailed riveting process simulation, virtual joint unit tests and the final large-scale model calibration. The virtual tests were simulated by detailed solid-element FE models of the joint-unit. These detailed models were validated using experimental tests, namely peeling, single-lap joint and cross tests. The virtual parameter calibration was compared to the experimental calibration and finally applied to component test simulations. The paper contains both experiments and numerical models to characterise the mechanical behaviour of the SPR connection under large deformation and failure.

Keywords: Self-piercing rivet, virtual testing, multi-sheet, multi-scale, aluminium.

1. Introduction

Car body structures are made from a variety of components and materials, where each part is designed and placed to fulfil its purpose. The final geometry of the components and the choice of materials are the result of an iterative design process. Modern design philosophies advocate the integrated use of dissimilar materials including steel and aluminium sheets, polymers and foams, as well as metal extrusions and castings [1, 2]. This multi-material design strategy holds particular significance for

*Corresponding author.

Email addresses: victor.andre@ntnu.no (Victor André), miguel.costas@ntnu.no (Miguel Costas), magnus.langseth@ntnu.no (Magnus Langseth), david.morin@ntnu.no (David Morin)

lightweighting in cars, and especially for electric vehicles. Different material qualities and part geometries usually require a tailored joining technique. Each car body structure has a large number of different combinations of material qualities and material thicknesses, each demanding its own suitable fastening techniques. A well-established fastening technique for the joining of aluminium sheets is self-piercing riveting (SPR) [3].

SPR connections are a popular choice as they do not require pilot drilling of the sheets and can therefore be placed automatically in assembly line production [4]. A semi-tubular rivet is pushed into a material stack; as the rivet deforms, it locks the sheets in place, creating a spot-like connection. Multiple SPR connections are often placed as a seam on component edges, also in combination with structural adhesive [5]. Most SPR connections are made between two mating sheets. However, connections can also be made up of multiple sheets, leading to more complex design possibilities and enabling further lightweighting potential using multi-material systems.

During the design process of SPR connections, manufacturability as well as correct mechanical performance must be ensured. Strength, failure and fatigue behaviour are particularly important [6]. The connections greatly contribute to the structural stiffness of the car, and moreover have a significant influence on the deformation of components under events like crash and impact. In order to meet worldwide crash regulations, the car body must behave in a predictable and safe manner. The design of full-car body structures and their components employs powerful numerical tools like the finite element method (FEM).

With respect to the SPR connection design, FEM can be utilised at different scales. Process simulations facilitate the creation of SPR geometries, enabling the assessment of joint quality through measures such as interlock or by computation of the riveting force. Process simulations are also the basis for detailed solid element models. Recent studies on SPR process modelling have been presented by Fang et al. [7], Kappe et al. [8] and Zhao et al. [9]. To study the mechanical behaviour of SPR during severe loading, detailed simulations with solid elements are used, as presented by

Hirsch et al. [10], Hönsch et al. [11] and Karim et al. [12]. To reduce the computational effort, surrogate models are used in shell-element-based car crash analyses as shown recently by Duan et al. [13], Leconte et al. [14] and Wang et al. [15]. Under defined conditions and with sufficient knowledge of the material's constitutive behaviour, mechanical SPR characterisation tests can be modelled [16]. As the mechanical characterisation of SPR connections is time and material-consuming, these virtual tests offer great potential. Virtual testing allows for the optimisation of tool geometry and material pairing, easing the testing of multiple joint configurations in the early development phase and aiding in the screening of possible design choices [17].

Surrogate or connector models applied in large-scale car crash simulations often require various experiments for calibration [14]. These calibration experiments can to some extent be replaced by detailed simulations of the SPR connection. Detailed simulations of the joint are further referred to as mesoscopic simulations/models, where 3D solid elements are used to discretise the rivet and sheet material. Connector models used in full-scale car crash simulations are further referred to as macroscopic models. Macroscopic models use shell elements to discretise the sheet material, where the element size is equal to or larger than the size of the SPR. Therefore, the detailed geometry of the SPR cannot be modelled using said large shell elements. Instead, the connector model is used to reproduce the force-displacement behaviour of the joint.

Limited work has been published on the large-scale modelling of three-sheet SPR connections. Process simulations followed by virtual calibration tests of large-scale shell connector models are rare. Since three-sheet connector models require more tests than two-sheet connections, a virtual calibration procedure is attractive. Therefore, this work presents a novel approach for a virtual calibration strategy and its experimental validation for an SPR connection between three aluminium sheets. The individual steps throughout the calibration procedure are not novel in themselves and can be replicated. The work involves calibrating models based on material and joint tests, with each stage of the process being experimentally validated, including component tests.

2. Calibration framework

The virtual calibration strategy proposed in this work had four main steps and is depicted in Fig. 1. The first step involved the material characterisation and constitutive modelling for both mesoscopic and macroscopic simulations. In addition, cross section cuts of the SPR connection were made in order to evaluate the accuracy of the following riveting process step.

The process simulation allowed for a fast creation of the connector geometry using axisymmetric 2D models, which included the known rivet and die geometries as well as the constitutive material models. This process simulation produced the SPR connection geometry including the resulting plastic strain and work hardening history. By adjusting process parameters such as friction coefficients and riveting speed, a close fit to the physical section cut could be achieved. The friction coefficient between the top-middle-sheet, middle-bottom-sheet, bottom-sheet-die and rivet-top-sheet pairings was tuned to optimise the fit between the physical section cut and the deformed mesh contour. The LS-OPT software was used to tune the process parameters to achieve minimum error between experimental and simulated rivet quality measures. The rivet quality measures were: sheet interlock, rivet spread and compression, as further described in Section 2.1.

A solid element model of the SPR connection was generated from the resulting geometry and incorporated into mesoscopic cross test models. Then, these mesoscopic cross test models were validated by peeling, single lap joint (SLJ) and free middle sheet cross tests. The responses from the mesoscopic cross tests are referred to as virtual cross test results.

A parallel large-scale model calibration was done using the experimental cross test to compare against the virtually calibrated models. The parameter set for the experimentally calibrated model was taken from André et al. [18].

The macroscopic models including the calibrated connector models were validated by peeling, SLJ and free middle sheet cross tests. The selection of these tests was motivated by their non-proportional loading mode, which poses a greater challenge to the model compared to the cross tests, which give an almost proportional loading. In addition, these tests do not enforce failure of a specific sheet since the middle sheet is unclamped. Finally, the interaction effects of multiple three-sheet SPR connections on a large-scale level were investigated with a component test. The macroscopic connector models were thereby challenged and the differences between the experimentally and the virtually calibrated models on the global component behaviour were evaluated.

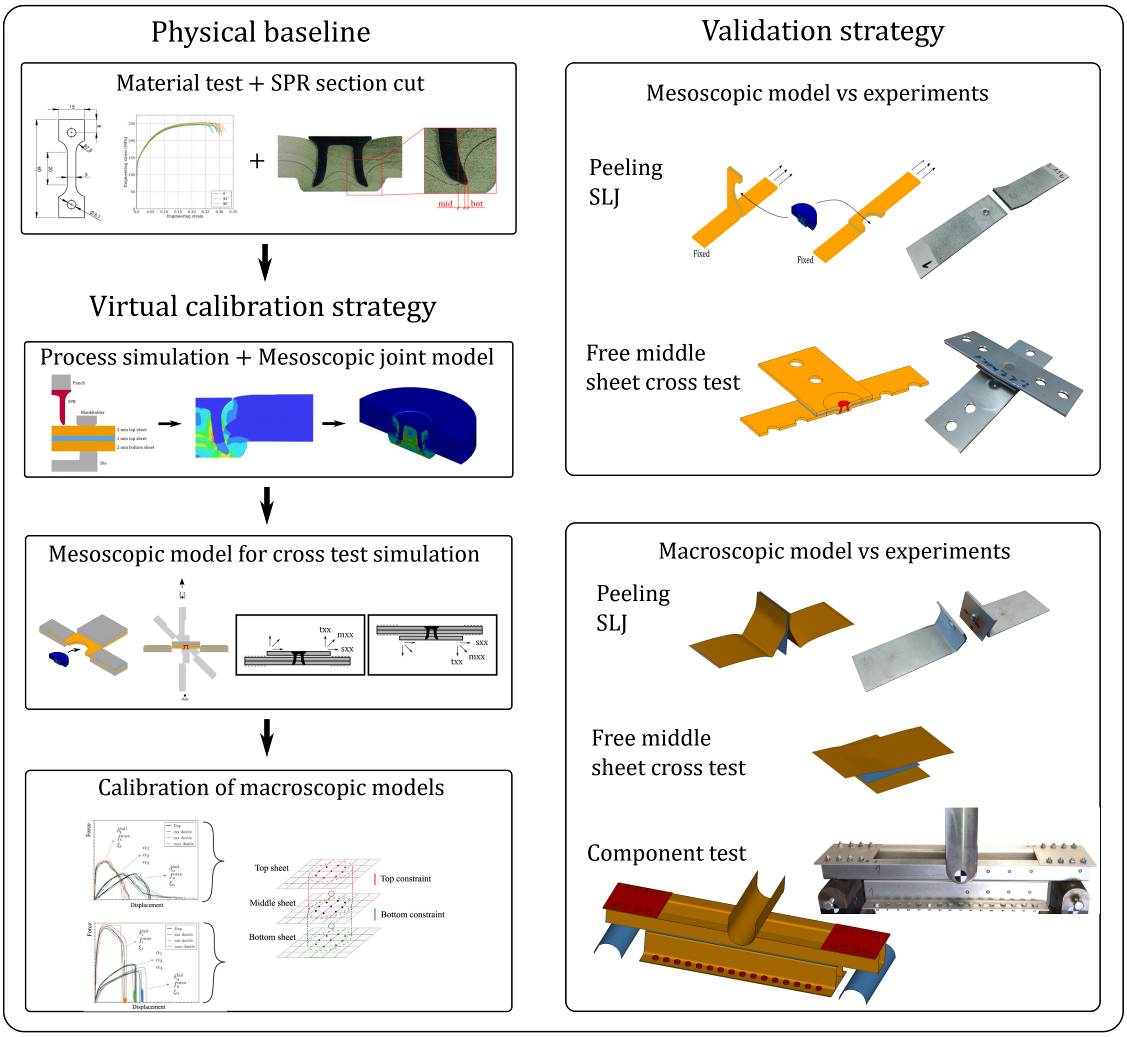

Fig. 1. Calibration and validation strategy / overview

2.1. *Strategy overview*

The presented calibration strategy is applied to a SPR connection made from three AA6016 aluminium sheets in T4 temper condition and a rivet from type Böllhoff RIVSET K 5.3×7. The aluminium sheets where stacked with a 2 mm thick sheet on the top and bottom and a 1mm thick sheet in between, resulting in a total stack thickness of 5 mm. A section cut of the resulting joint is shown in Fig. 2. The rivet had a shank diameter of 5.3 mm, the head diameter was 7.75 mm and the overall rivet length was 7 mm, as shown in Fig. 2. The riveting die was shaped with a flat bottom and a diameter of 11 mm. This joint SPR configuration was studied by André et al. [18] where the effect of different sheet stack-ups on the joint behaviour was investigated.

For two-sheet SPR connections, usually the interlock between rivet and bottom sheet is measured, which is a practical quality criterion [2]. The bottom interlock is defined as the radial distance between rivet tip and bottom sheet tip which folds inwards around the rivet tip. A high interlock measure is usually a good indicator for a strong mechanical connection between the bottom sheet and the rivet. For the three-sheet connection, an additional interlock for the middle sheet was defined, as displayed in Fig. 2. The middle interlock was defined as the radial distance between bottom sheet tip and inner edge of the middle sheet. Rivet spread and compression are the differences between deformed and undeformed rivet geometry measured at the rivet tip. A bottom-sheet interlock of 0.22 mm ("bot" Fig. 2) and a middle-sheet interlock of 0.40 mm ("mid" Fig. 2) were measured. In the section cut, the rivet got compressed by 0.80 mm ("comp" Fig. 2) and the tip of the legs were spread out by 0.74 mm ("spread" Fig. 2).

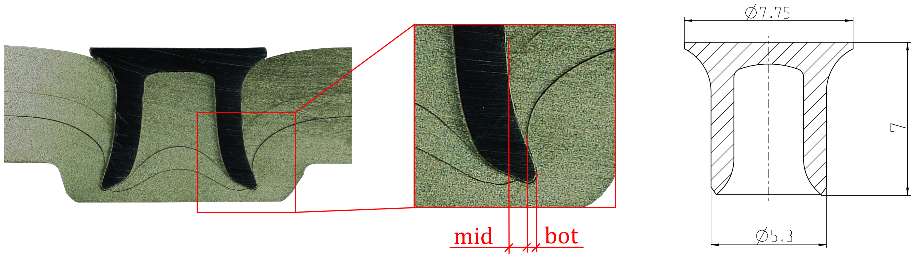

Fig. 2. SPR section cut with interlock, compression and spread measures.

2.2. Sheet material characterisation

The mechanical properties of the rolled AA6016-T4 sheets were experimentally characterised. Tensile specimens with the dimensions given in Fig. 3a were extracted from the sheets in 0°, 45° and 90° with respect to the rolling direction. Four specimens were extracted for each sheet thickness in each direction, which resulted in a total of 24 tensile specimens. Dimensional accuracy was ensured by cutting the specimens using wire erosion in a water bath, making sure the aluminium was not affected by heat. The tensile tests were carried out at room temperature, 0.02 mm/s and recorded at 1 frame/s with a Basler acA4112 camera and an approximate resolution of 80 px/mm. The specimens were loaded with an Instron 5982 universal testing machine and a 100 kN load cell. The specimens were painted with a black-and-white speckle pattern and the surface deformations were computed using digital image correlation (DIC) with the software eCorr [19]. A digital extensometer with a gauge length of 18.38 mm was used to obtain the engineering strains. The determined stress-strain curves are displayed in Figs. 3b and 3c for the two thicknesses, respectively. No significant difference in yield stress, work hardening and failure was observed for all the directions. The higher strength of the 1 mm sheet could be an effect of the thinner rolling but was not further evaluated.

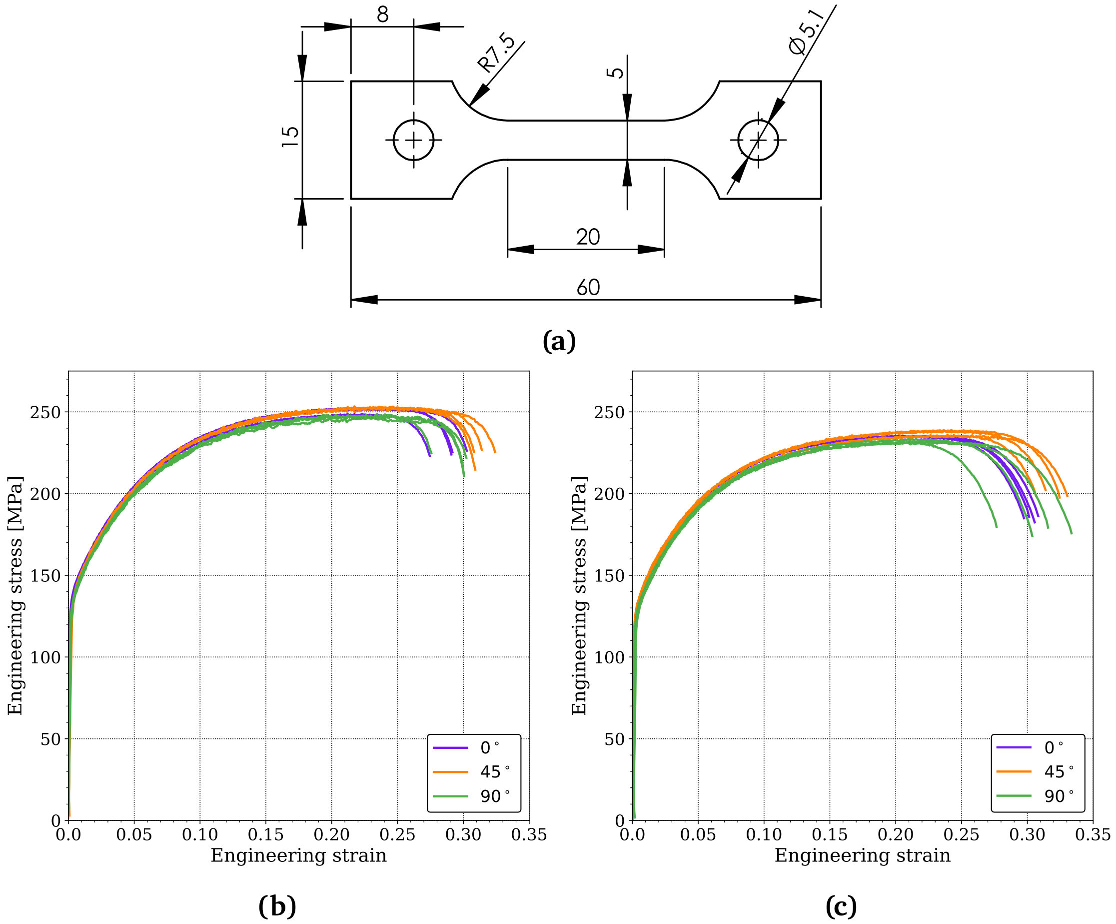

Fig. 3. Tensile test: (a) specimen dimensions in mm, (b) 1 mm sheet and (c) 2 mm sheet.

2.3. Rivet material characterisation

The rivet material was characterised by axial compression of the rivet body between two flat surfaces without lubrication. Material characterisation by crushing of the rivet body, previously presented by Khezri et al. [20], Porcaro et al. [21], Baha II [22] and Hönsch et al. [23], was simplified in this work by testing the original rivet without additional machining. The deformation sequence is displayed in Fig. 4a and a bulging of the rivet's midsection could be observed. DIC was used to track the punch displacement applying the eCorr [19] point tracking algorithm. Three repetitions were carried out under quasi-static conditions and the force-displacement curves can be seen in Fig. 4b. The results were repeatable and the response curves were used for later material model calibration through inverse engineering.

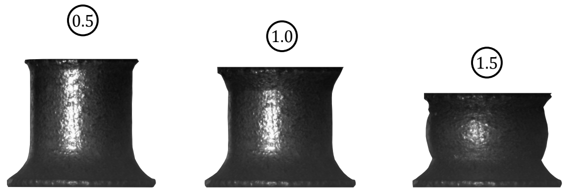

(a)

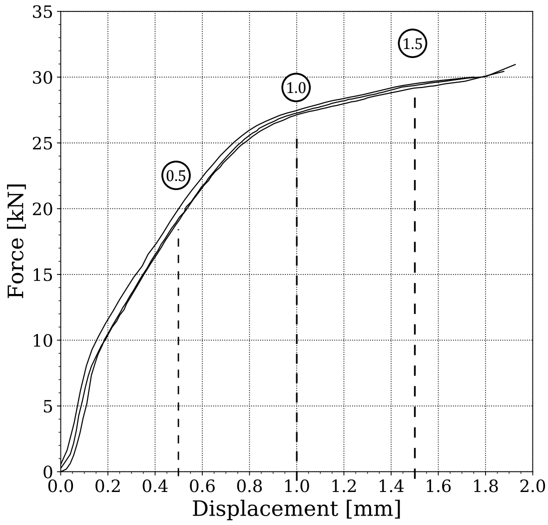

(b)

Fig. 4. Rivet compression test: (a) deformation at 0.5, 1.0 and 1.5 mm compression, (b) force-displacement response.

2.4. SPR joint characterisation

The SPR connection investigated in this work was experimentally tested in André et al. [18], where the joint unit was characterised by cross tests under six loading modes. Either the top sheet was loaded and the middle and bottom sheets were clamped or the bottom sheet was loaded and the top and middle sheets were clamped. By rotating the clamps in the test rig, different loading modes were achieved, see Fig. 5a. Either the top or bottom sheet was loaded under pure tension, pure shear and mixed mode. The joint loading modes are depicted in Figs. 5c and 5d and are referred to as txx, sxx and mxx for top sheet tensile, shear and mixed mode loading. Bottom layer tension, shear and mixed mode loading are abbreviated with xxt, xxs and respectively xxm.

Each loading configuration was tested with five repetitions resulting in total 30 tests. Fig. 6 shows the resulting force-displacement curves. Two distinct failure modes were observed. Rivet-pull-through was defined as the top sheet extracting the rivet

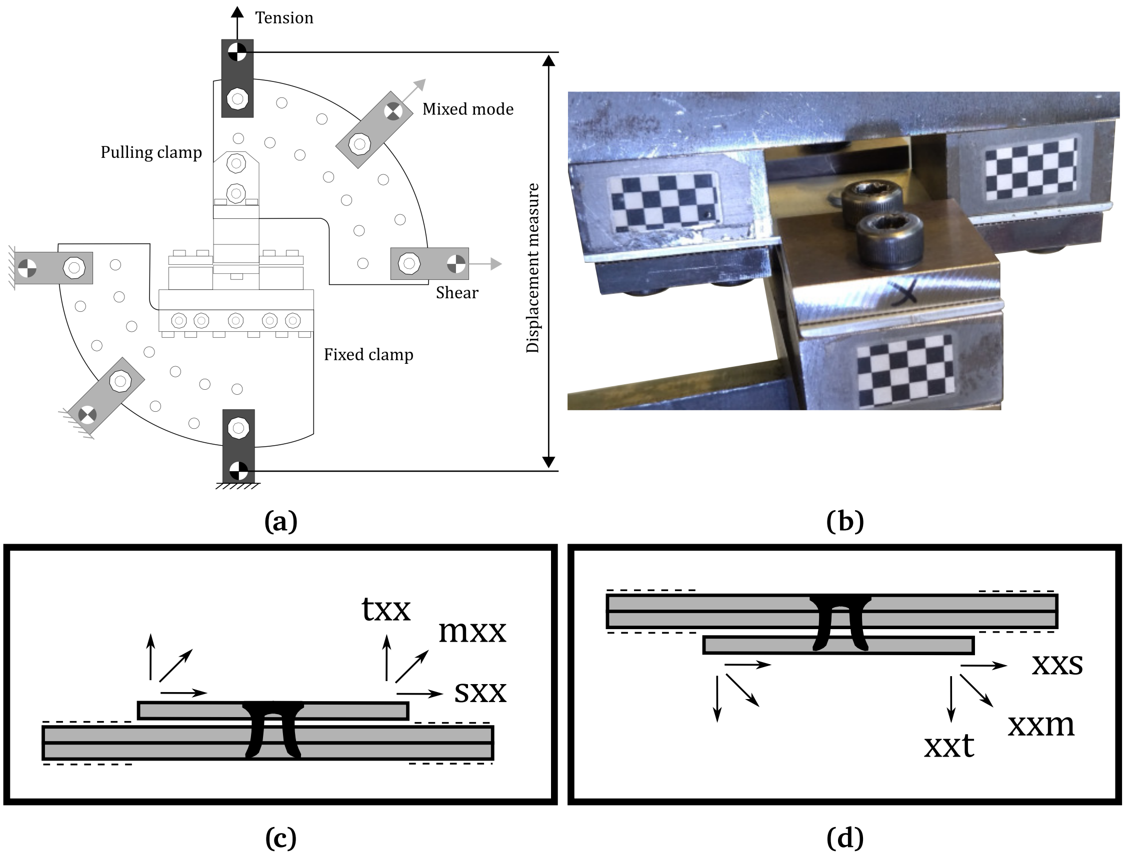

Fig. 5. Cross test: (a) schematic test rig, (b) clamping, (c) top sheet loading and (d) bottom sheet loading.

body, leading to the full separation of all sheets. Rivet-pull-out was defined as the case where the bottom sheet detached from the rivet while the top and middle sheets were still connected. The assignment of the failure modes to the cross test loadings is displayed in Fig. 7.

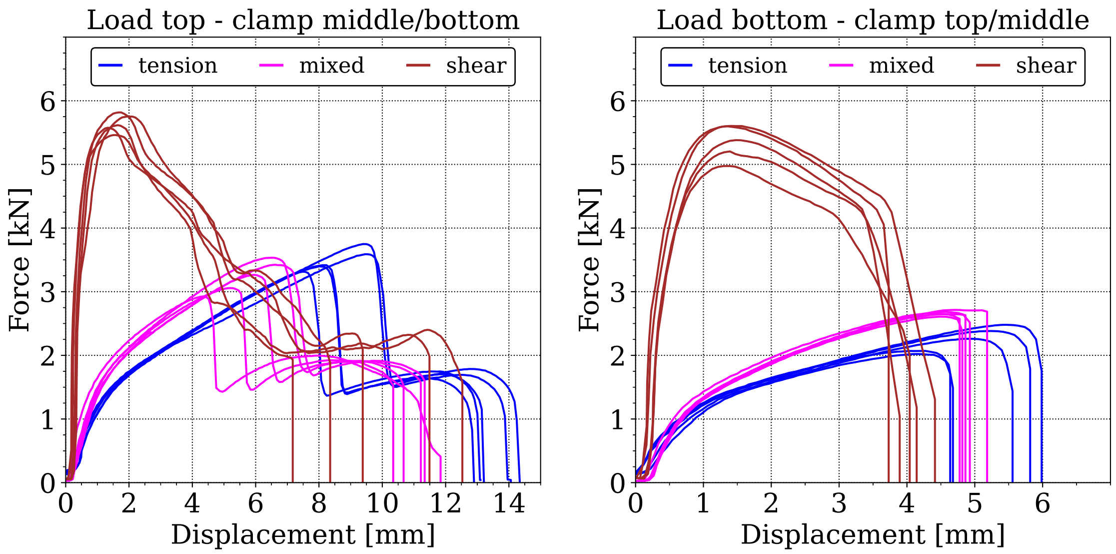

Fig. 6. Experimental cross test results.

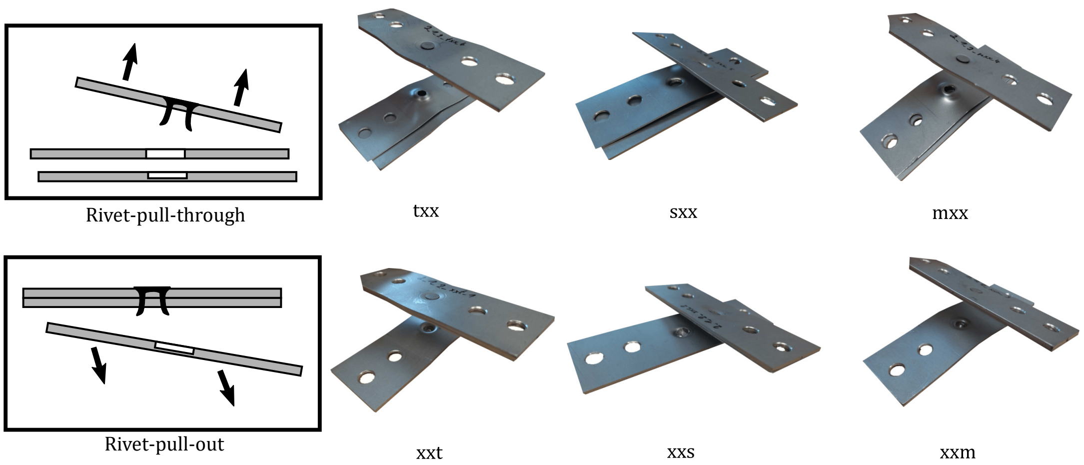

Fig. 7. Assigned cross test failure modes

3. Mesoscopic modelling

3.1. Constitutive modelling for process and mesoscopic modelling

For both the aluminium sheet and the rivet an isotropic plasticity material model was applied. The *MAT_PIECEWISE_LINEAR_PLASTICITY keyword in LS-DYNA [24] was used which offers the von Mises yield criterion with isotropic hardening. The hardening for the aluminium sheets was modelled by the Voce hardening rule according to Eq. (A.3). A combination of power-law and Voce hardening was used to model the work-hardening behaviour of the rivet material as described by Eq. (A.5). The governing equations for the constitutive modelling are supplied in Appendix A.

The flow curves generated from the hardening rules Eq. (A.3) and Eq. (A.5) were supplied in tabulated form and the evolution of true stress over true plastic strain for the sheet and the rivet material are shown in Fig. 8a and Fig. 9a, respectively. Damage in the aluminium and the rivet material was not modelled as no fracture was observed in the cross tests. Thinning and splitting of the aluminium sheet in the process simulation was modelled by adaptive remeshing.

The response curves from the inverse solid element models of the tensile test and the rivet compression test are shown in Fig. 8b and Fig. 9c. The simulations of the sheet tensile tests showed good agreement with the experiments and the material model was able to capture the necking behaviour. The hardening model for the rivet material allowed for the capture of the initial stiffness of the rivet compression tests with slight deviation for larger punch displacements. As none of these extensive deformations occur in the process simulation and the mesoscopic models, the curve fit as seen in Fig. 9c is sufficient. The hardening parameters for the rivet material are given in Table 1. The compression test simulation was therefore stopped at 1.8 mm. A friction coefficient of 0.15 was chosen between the rivet and the punches giving a similar deformation mode with bulging of the rivets mid section replicated by the simulation, depicted in Fig. 9b. It should be noted that the friction coefficient might change the stiffness and deformed shape of the rivet under compression.

Table 1. Material parameters for rivet

E (GPa)	ν (-)	σ_0 (MPa)	Q (MPa)	H (MPa)	c (-)
210.0	0.30	1302.2	443.9	314.3	82.1

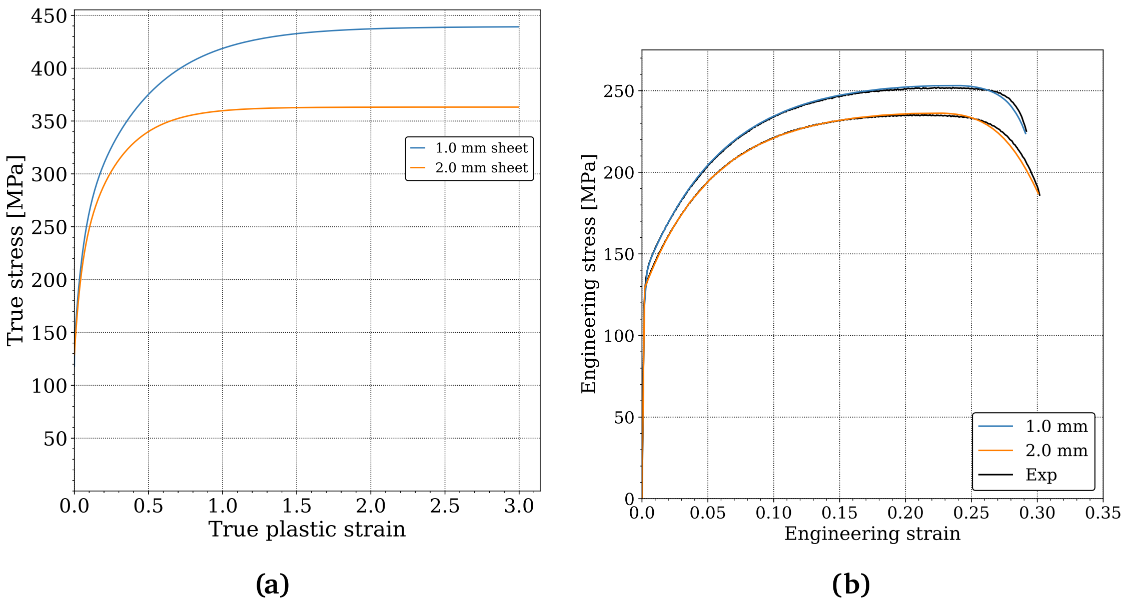

Fig. 8. Aluminium material calibration: (a) extrapolated flowcurves, (b) inverse tensile test modelling results.

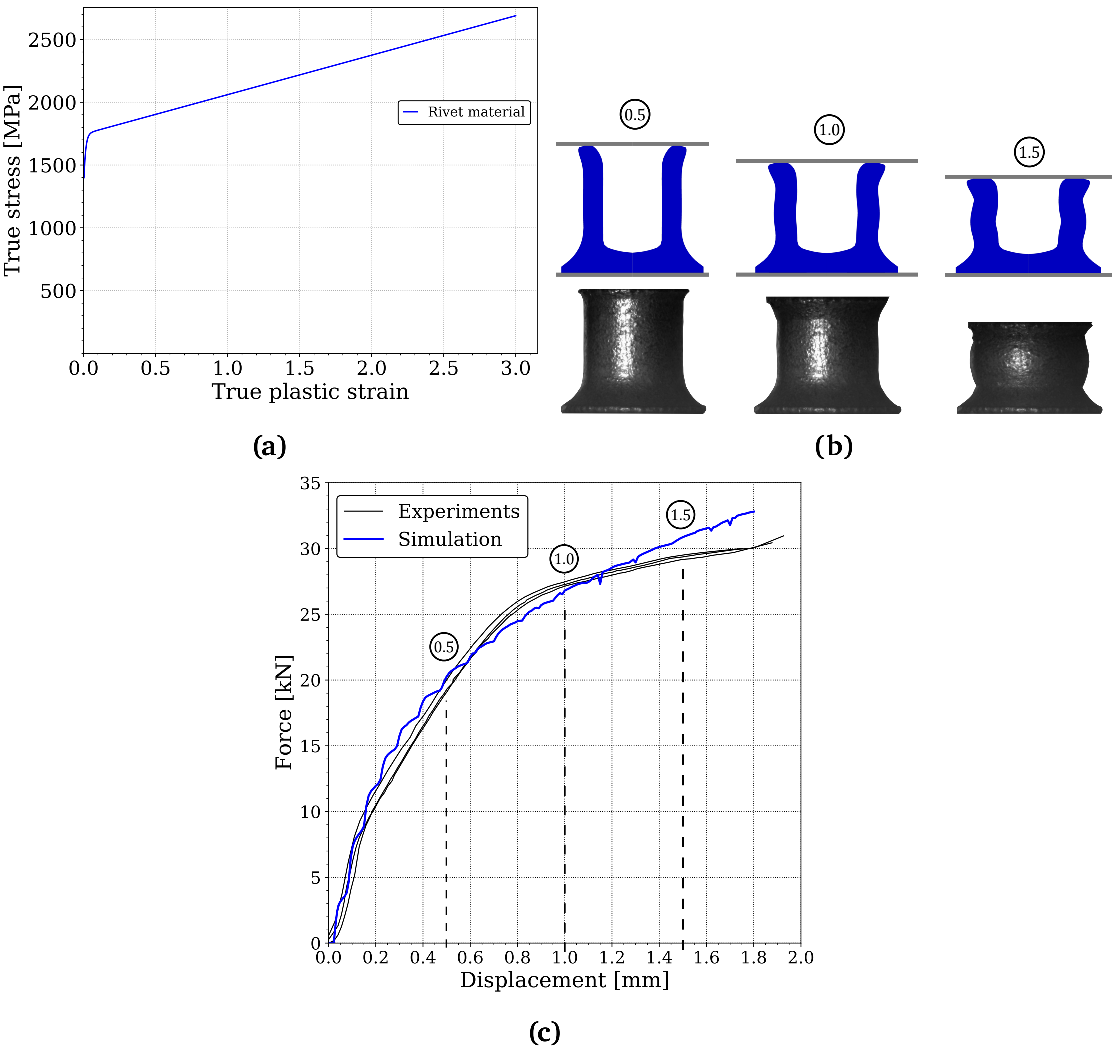

Fig. 9. Rivet material calibration: (a) extrapolated flowcurve, (b) deformation sequence simulation vs experiment and (c) inverse rivet compression model response.

3.2. *Riveting process simulation and virtual cross testing*

The SPR riveting process was modelled in the explicit LS-DYNA solver version 11 [24] using a 2D axisymmetric model. Many studies have been published on the suitability of 2D models for the riveting process. A reduction of numerical costs can thereby be reduced as shown by Porcaro et al. [21] for the modelling of two-sheet aluminium SPR connections. Bouchard et al. [25] and Karathanasopoulos et al. [26] presented the successful application of 2D axisymmetric models for hybrid aluminium and steel SPR joints. The process modelling of three-sheet aluminium SPR connections was shown by Mori et al. [4]. According to Moraes et al. [27], the simulated rivet interlock as a key feature of the SPR joint is greatly influenced by the coefficients of friction between the sheets and the die. Multiple simulations with adjustment of the friction parameters were therefore necessary to find the modelled joint interlock that matched the physical cross section. Multiple options for modelling material fracture are available including simple minimum thickness criteria or complex constitutive models. However, according to Huang et al. [28], an inappropriate failure criterion can lead to unrealistic volume loss or incorrect crack growth, which can cause a deviation between the experimental and simulated joint cross-section and rivet force.

The riveting process begins with the sheets being clamped between die and blankholder Fig. 11a. The punch pushes the rivet into the sheets where the rivet legs penetrate and bend outwards to plastically deform, locking the sheets together. When the rivet head is approximately flush with the top sheet surface, the punch and blankholder retract.

The riveting process model consists of deformable parts, namely the rivet body and the three sheets. Punch, blankholder and die were modelled as rigid bodies. All parts where discretised using four-node volume weighted axisymmetric solid elements. As the sheet material experiences severe plastic deformation, an adaptive remeshing algorithm was applied to overcome excessive element distortion. The rivet and sheet materials were modelled using the isotropic plasticity model described in Section 3.1. In these simulations, the effects of strain-rate and temperature due to adiabatic conditions were not accounted for. Modelling of material damage was not accounted for as element erosion could lead to problems in the contact formulation and eventually to an aborted simulation. Material failure due to sheet piercing was modelled using the part adaptive failure keyword from LS-DYNA. This feature allows for the splitting of a sheet into two parts based on a critical thickness, thus creating two new surfaces without deleting elements [21]. The remeshing steps where sufficient to account for the thinning and splitting of the sheet material. A 2D penalty based Coulomb friction formulation was used between the parts. Because the punch displacement, the punch velocity and the friction coefficients have significant influence on the final joint geometry, several iterations with adjustment of parameters was necessary to achieve the optimal geometry.

The resulting mesh contour is displayed and compared to the physical section cut in Fig. 10. This shape was achieved using a friction coefficient of 0.31 between the sheets, friction coefficient of 0.36 between sheets and die and almost no friction between the rivet and the sheets with a coefficient of 0.08. The friction parameters were found to give a good fit between physical cut and mesh geometry measured by the variables in Table 2. As seen in the table, a higher rivet compression and spread than in the physical cut was achieved. While the bottom interlock was underestimated, the middle interlock showed a higher value than in the physical cut. These values provided the best results in the cross-test simulations, even though they show a relatively large error in Table 2.

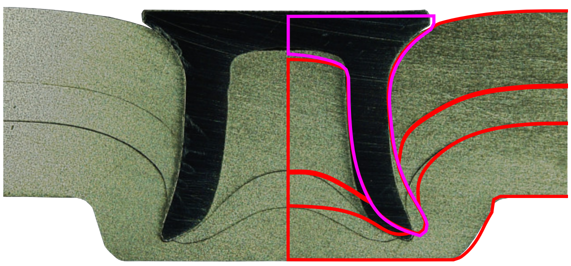

Fig. 10. SPR section: physical cut vs mesh contour.

After the 2D process simulation, the deformed mesh geometry of rivet and sheets was extracted while storing the equivalent plastic strain and work hardening for each

Table 2. Riveting process quality measures in mm.

	Rivet compression	Rivet spread	Bottom interlock	Middle interlock
Physical cut	0.80	0.74	0.22	0.40
Mesh contour	1.19	1.03	0.17	0.54
Error	49 %	39 %	23 %	35 %

element, Fig. 11b. A 3D solid mesh was generated by rotation of the shell elements in 20 angular increments Fig. 11c, Fig. 11d. The resulting model unit was inserted in a cross test specimen mesh, Fig. 11e, further referred to as a mesoscopic model.

Two different mesh configurations were used where either the top-loaded sheet or the bottom-loaded sheet were placed transversely to the two clamped sheets. The sheet meshes were sandwiched between rigid bodies replicating the cross test setup shown in Fig. 11f. The tests were modelled using a symmetry plane to reduce the computational costs. The mixed mode and shear cases incorporated a half-sized clamp for clearance of the moving sheet. Each clamp was made from two solid parts which were held together with beam elements, modelling the initial clamp tightening and allowing for slight opening of the clamp Fig. 11g. The clamping load was applied with an initial axial force in the clamping beam elements. The pre-load in the beams was 8 kN which was assumed from the hand tightening of the real M8 bolts. Different axial pre-loading values showed no significant differences in the clamping behaviour. The contact between clamps and sheets was realised by a penalty-based Coulomb friction model with a friction coefficient of 0.25 allowing for minimal sliding during the test.

The resulting force-displacement curves from the mesoscopic cross test simulations are given in Fig. 12 and are compared to the experiments. The models were able to capture the overall curve shape for each loading mode with a good agreement of both peak force and displacement to failure. However, the models of the shear loadings overestimated the peak force, especially in the bottom layer loading xxs. The modelling of sheet material damage and element erosion around the rivet could have decreased the strength but was not evaluated further. All simulations predicted a stiffer joint response than experiments, especially in the bottom layer loading modes.

However, all models reproduced the failure modes as observed in the experiments, which can also be seen by the matching drop in force in the txx and mxx tests where middle and bottom layer separated around the rivet. The discrepancies observed in the mesoscopic simulations of the cross-tests are believed to be associated with the deformed geometry of the rivet and surrounding sheets obtained through the process simulations.

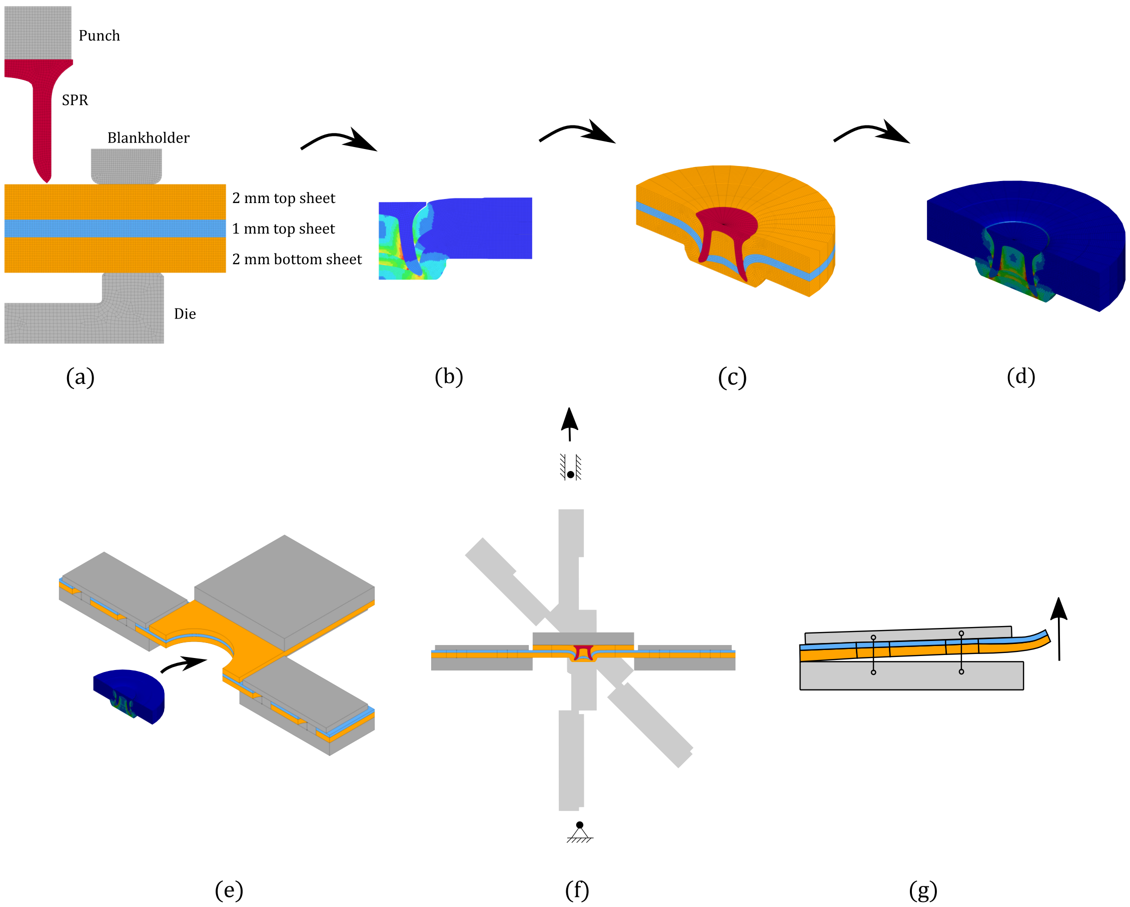

Fig. 11. Mesoscopic model generation: (a) 2D riveting process, (b) resulting 2D mesh, (c) solid element mesh, (d) plastic strain mapping, (e) cross test model, (f) hinged cross test rig model and (g) clamping setup.

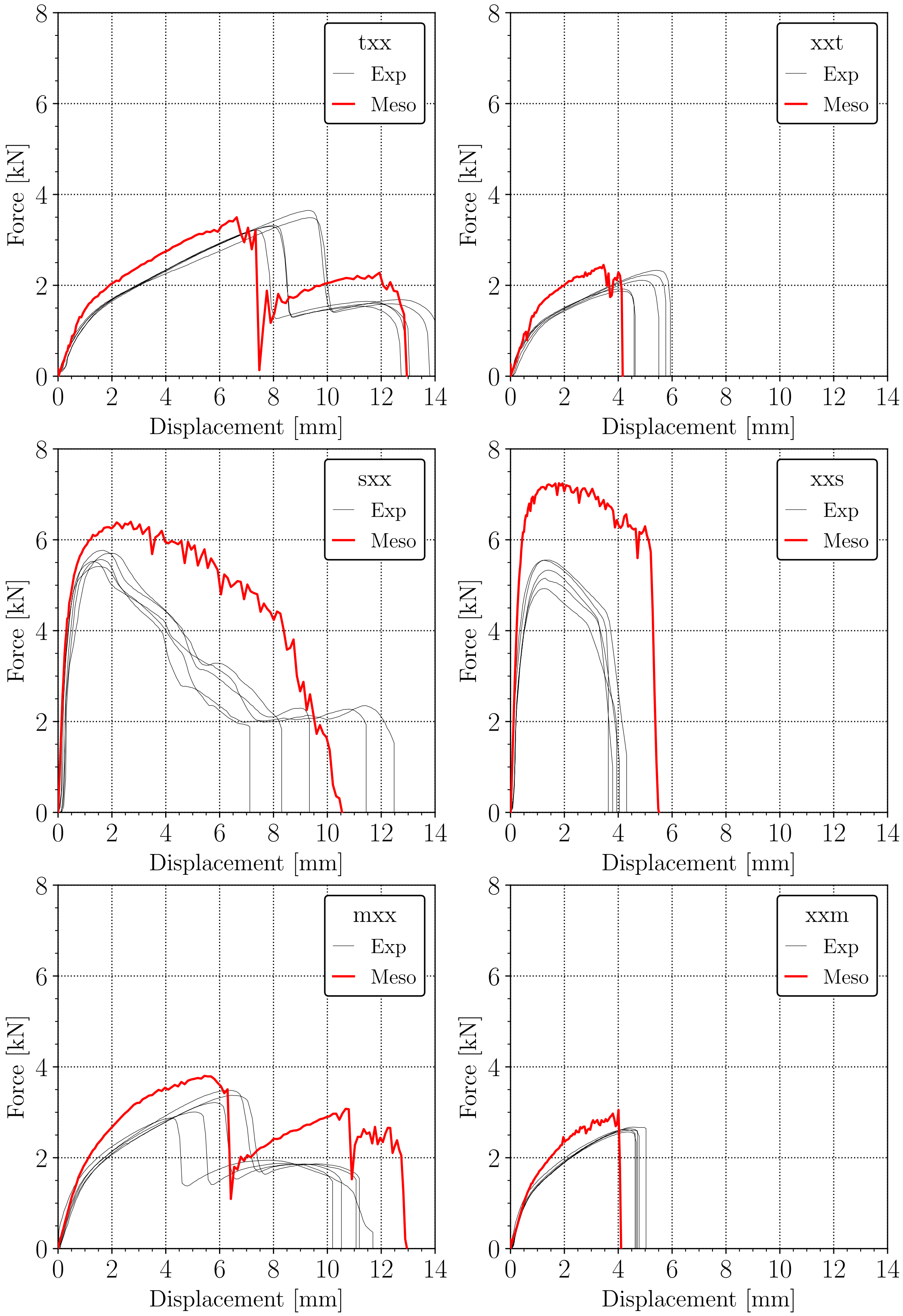

Fig. 12. Force-displacement curves of the mesoscopic cross tests vs the experiments.

4. Macroscopic modelling

4.1. Constitutive modelling for shell elements

The shell-element discretised aluminium sheets in the macroscopic simulations were modelled with an isotropic plasticity model. The Hershey-Hosford yield criterion [29] and Voce-hardening were adopted. The model is based on the work by Costas et al. [30] and is available as *MAT_258 keyword in the explicit LS-DYNA solver [24]. The work hardening parameters were taken from [18] and the obtained simulation response is displayed in Fig. 8b. The Voce-hardening parameters were originally obtained from the tension tests in 0° direction and are shown in Table 3. That results in two individual material cards for the 1 mm and the 2 mm sheet material.

Table 3. Material parameters for AA6016 in T4 temper

Sheet thickness (mm)	E (GPa)	ν (-)	σ_0 (MPa)	θ_{R1} (MPa)	Q_{R1} (MPa)	θ_{R2} (MPa)	Q_{R2} (MPa)	θ_{R3} (MPa)	Q_{R3} (MPa)
1.0	70.0	0.33	115.3	26919.2	22.7	1831.9	102.2	451.9	199.3
2.0	70.0	0.33	128.7	1362.4	59.4	604.4	157.6	403.0	17.6

4.2. Macroscopic connector modelling

Modelling of the SPR in large-scale macroscopic models was realised by a connector model. In this work, the connector was modelled by the constraint formulation proposed by Hanssen et al. [31], which is available as *CONSTRAINED_SPR2 keyword in the explicit LS-DYNA solver [24]. While the connector model was originally designed for connections between two sheets, André et al. [18] presented the application of two sandwiched connectors between three sheets for the modelling of three-sheet connections. The stacking of two connector models is sketched in Fig. 13.

One constraint was placed between each pair of shell element meshes and, depending on the relative nodal displacement of the sheets, the resulting forces and moments acting on the sheets were computed. The constraint model accounts for damage and scales down the forces while the state of maximum accumulated damage is stored. Each constraint model is governed by nine parameters which are usually

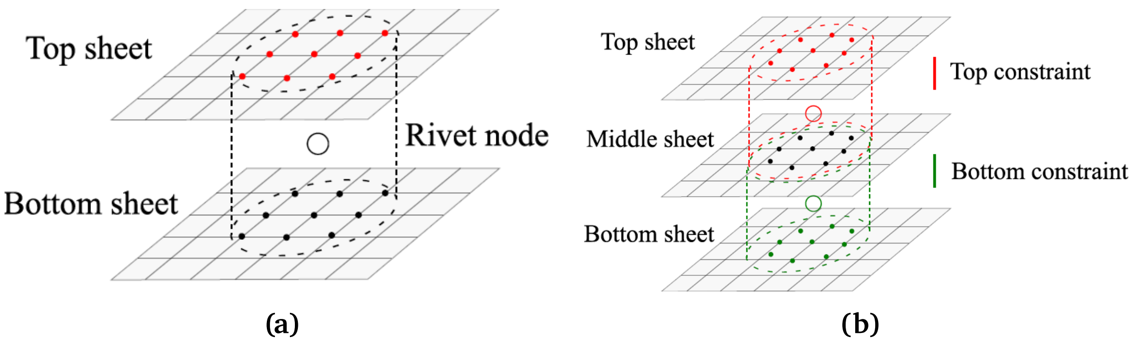

Fig. 13. Constraint modelling technique: (a) general two-sheet and (b) three-sheet connection.

fitted by inverse engineering. Governing equations for the constraint model are given in Appendix B. For in-depth discussion of the constraint model, the work by Hanssen et al. [31] is referred to.

The modelling strategy for three-sheet connections applies two stacked connector models which rely on the same constraint model formulation but are independent in the sense that they use two different sets of parameters. The two connector models are neither connected with each other nor can they communicate. Fig. 14 shows the proposed calibration process of the 18 parameters for the three-sheet connection. This method allows for a calibration using a reasonable amount of experiments, which are the six cross tests. The top sheet loading tests were used for calibration of the top connector model and the bottom sheet loading tests for calibration of the bottom connector, respectively.

4.3. Connector model calibration: experimental and virtual

With the aim of comparing the virtual versus the experimental calibration strategy, both connector models were calibrated by inverse modelling of either the physical cross tests or the virtual tests. The response curves from the experimentally calibrated macroscopic models are shown in Fig. 15. The cross test model response was in good agreement with the experiments. The parameters under pure shear loading were calibrated so that a conservative failure behaviour at lower shear displacement was achieved. Also failure under top sheet tension and mixed mode loading were calibrated conservatively to ensure failure at the first force drop. This ensures full

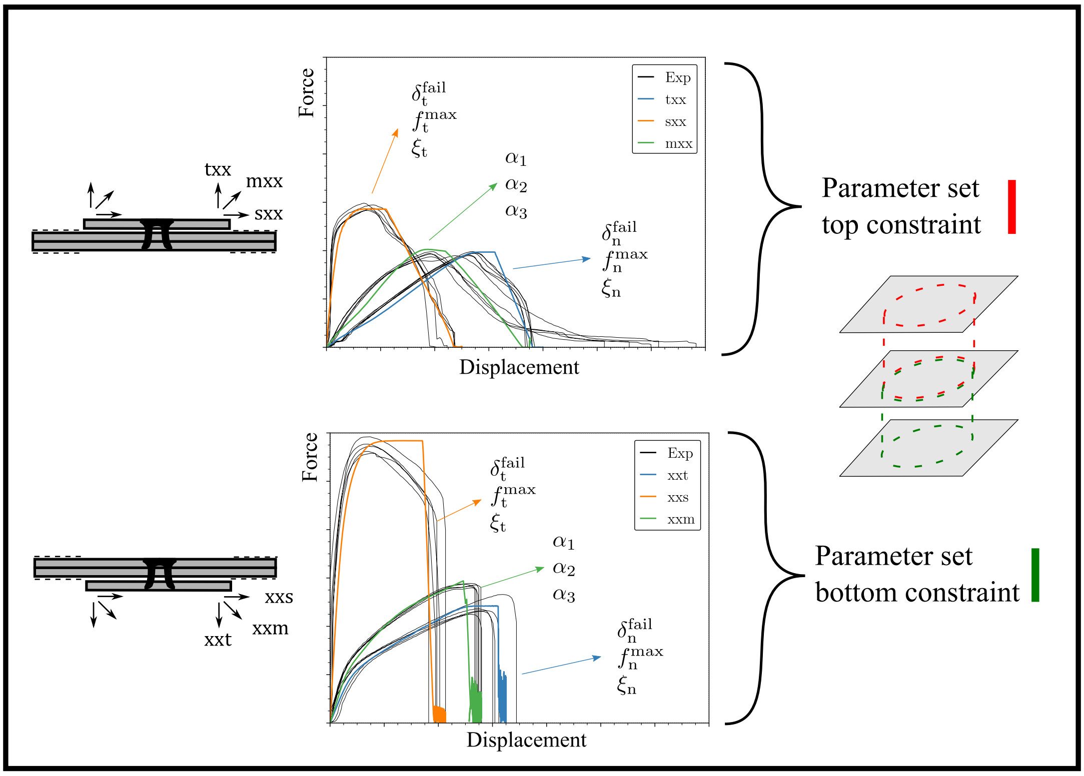

Fig. 14. Calibration process for each single constraint

separation of the top sheet from the clamped middle and bottom sheets.

Fig. 15 also shows the response from the cross test models with parameters found by inverse modelling of the virtual mesoscopic cross tests. The macroscopic simulations were in good agreement with the underlying mesoscopic model. Again, a more conservative parameter set was chosen to accomplish separation of the top sheet under top sheet tension and mixed mode loading. The response from the mixed mode and free middle sheet test showed deviation in force level and displacement to failure. The initial stiffness under shear loading could not be fully reached applying the virtually calibrated parameter set. Different rivet diameters were used for the virtually calibrated models to adjust the initial stiffness by increasing the diameter of influence and incorporating more nodes. The parameter sets are given in Table 4.

Table 4. Constraint model parameters. Experimental calibration obtained from [18].

Calibration	Constraint	$\delta_{\mathrm{n}}^{\mathrm{fail}}$ (mm)	$\delta_{\mathrm{t}}^{\mathrm{fail}}$ (mm)	$f_{\mathrm{n}}^{\mathrm{max}}$ (kN)	$f_{\mathrm{t}}^{\mathrm{max}}$ (kN)	ξ_{n} (-)	ξ_{t} (-)	α_1 (-)	α_2 (-)	α_3 (-)	Diameter (mm)
Experimental	Upper	3.149	3.566	3.392	5.801	0.749	0.705	0.804	0.750	1.489	10.0
	Lower	2.252	3.757	2.261	5.798	0.696	0.749	0.795	0.899	1.402	10.0
Virtual	Upper	2.956	10.356	3.392	6.253	0.749	0.350	1.171	0.386	0.437	15.0
	Lower	2.252	5.369	2.361	7.824	0.696	0.751	0.450	1.154	1.189	20.0

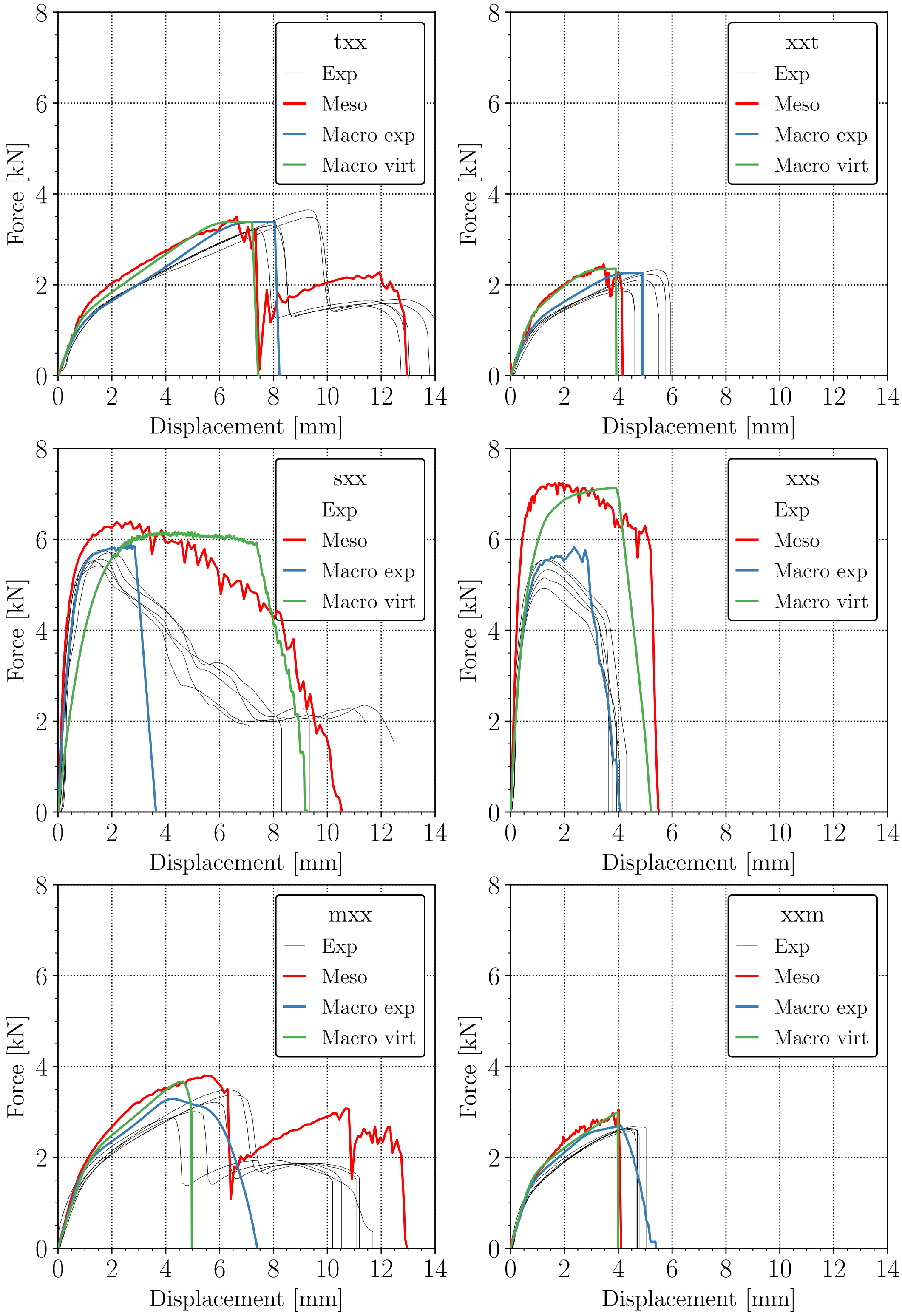

Fig. 15. Results from virtual cross tests, experimentally and virtually calibrated macroscopic models vs the experiments.

5. Strategy validation: Meso- and macroscopic models vs experiments

5.1. Benchmark tests and simulation

For the validation of the meso- and macroscopic models, three benchmark tests where conducted. The tests consisted of a cross test where the middle sheet was unclamped, a single-lap-joint (SLJ) test and a peeling test.

The free middle sheet cross test had the same dimensions as the regular cross tests but the middle layer was not clamped and was therefore a 40 × 40 mm square. The results from the free middle sheet test (labelled mox) are displayed in Fig. 16. The mesoscopic model and the experimentally calibrated macroscopic model showed a good representation of the experimental behaviour. The virtually calibrated macroscopic model captured the response from the mesoscopic model but overestimated peak force and failure displacement slightly.

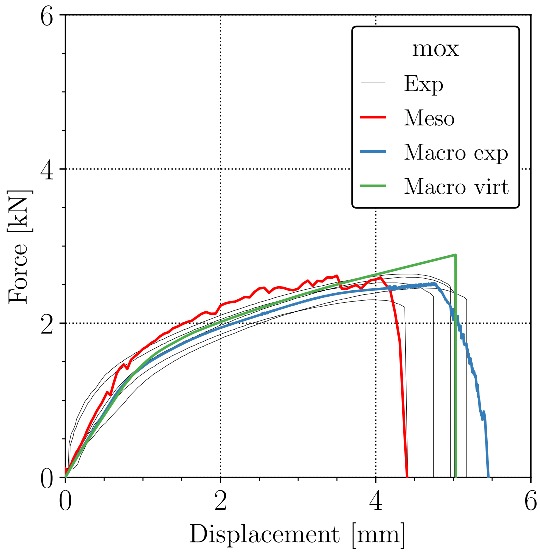

Fig. 16. Free middle sheet test: experiments “Exp”, mesoscopic model “Meso”, macroscopic model experimental calibration “Macro exp”, macroscopic model virtual calibration “Macro virt”.

The dimensions of the peeling and SLJ specimens are displayed in Fig. 17a and Fig. 18a with the clamping area marked in grey. In the cross test with unclamped middle-sheet, the top-sheet was loaded in mixed mode. Peeling and SLJ tests were done by clamping the bottom-sheet and moving the top-sheet, constraining both clamps in a straight line.

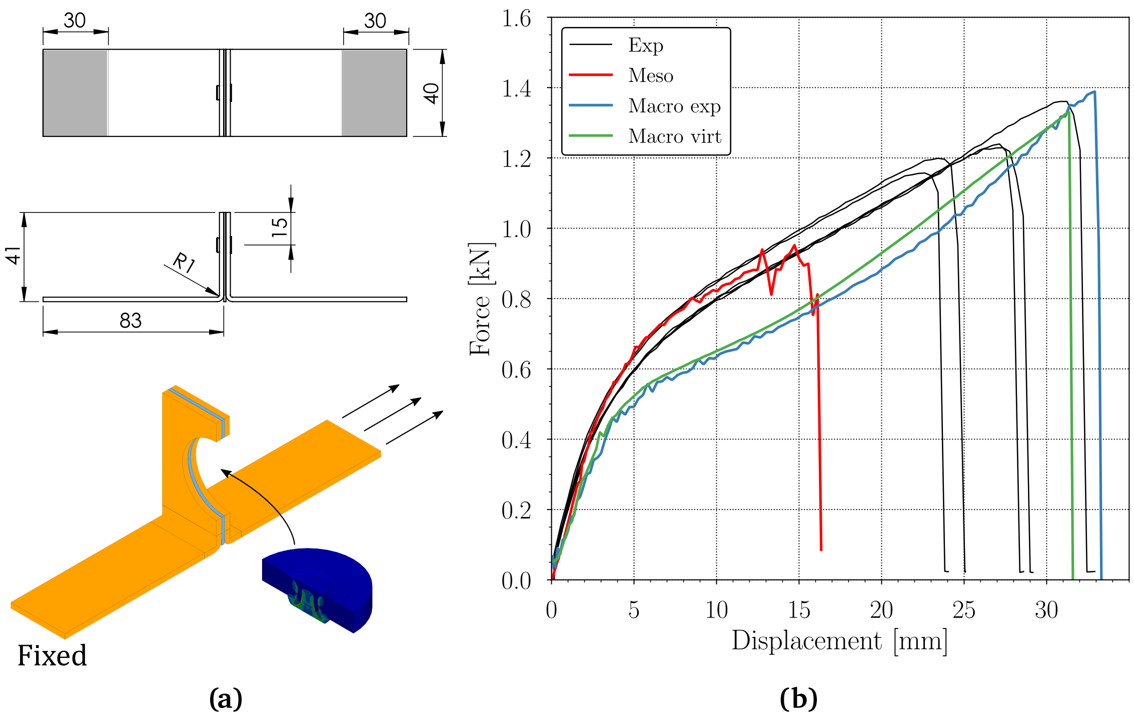

Fig. 17. Peeling tests: (a) specimen dimensions in mm, (b) force-displacement curves. Experiments “Exp”, mesoscopic model “Meso”, macroscopic model experimental calibration “Macro exp”, macroscopic model virtual calibration “Macro virt”.

The force-displacement curves from the peeling and SLJ test and models are displayed in Fig. 17b Fig. 18b.Slight scatter in the tests with a peak force ranging from 1.18 to 1.4 kN was observed. Displacement at failure was ranging from 24 to 32 mm. This could be related to minimal differences in the specimen manufacturing and rivet placement. The peeling specimens failed with the rivet-pull-out mode.

The resulting curves from the SLJ tests show a peak force ranging from 4.4 kN to 5.0 kN with a displacement to failure of 2.4 to 3 mm. Also the SLJ tests failed with the rivet-pull-out mode.

The mesoscopic model of the peeling test showed good agreement of the initial behaviour but fails at a lower peak force of approximately 0.9 kN and displacement of 15 mm. The deviation could be explained by the smaller bottom interlock in the mesoscopic model compared to the bottom. Additionally, the peel load introduced local bending and joint rotation, which lowered the displacement at failure compared to the mixed and tension loading modes. While the mesoscopic model of the SLJ tests showed a good representation of the peak force, the displacement to failure was overestimated by 0.5 mm.

The results from both the experimentally and the virtually calibrated macroscopic models were relatively similar. The macroscopic model of the peeling tests showed a lower force level in the initial loading but captured the peak force and failure displacement well. The SLJ model showed lower stiffness, matches the peak force but overestimates the failure displacement by approximately 1.7 mm.

Despite the deviation between the virtual cross test models and the cross test experiments, the virtually and the experimentally calibrated macroscopic models performed equally well in the peeling and SLJ simulations. Considering that both calibrations of the macroscopic model led to the same overall response, the general mismatch between the simulations and the experiments likely stems from the modelling of the SLJ experiments with shell elements. In these experiments, initially loaded in pure shear, the sheets may undergo rotation and slight bending which are difficult to capture with a shell element approach.

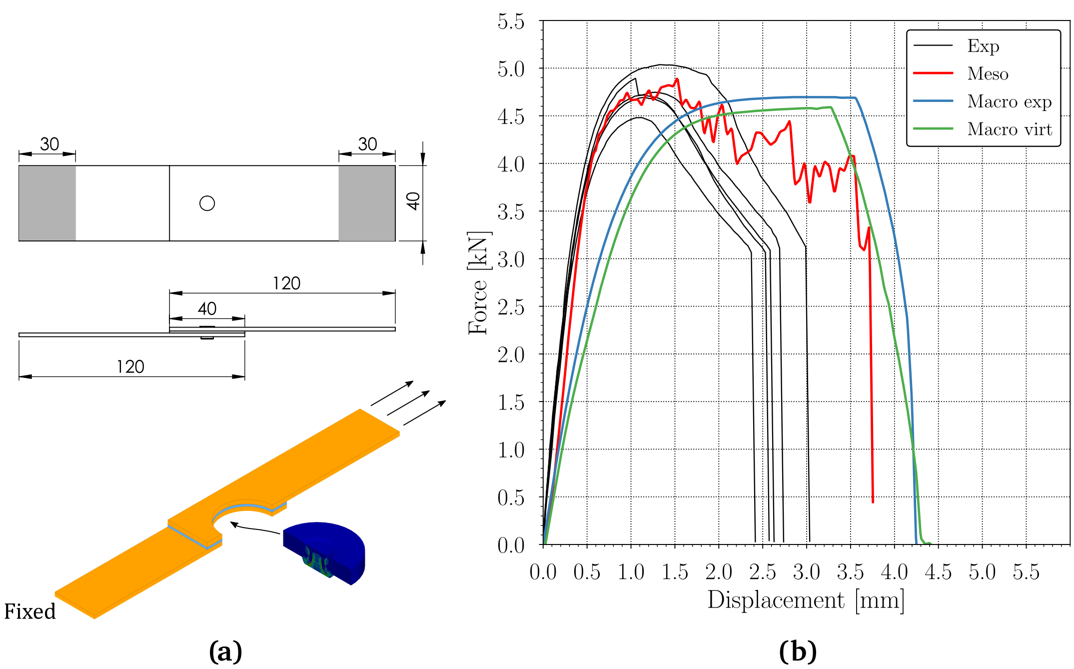

Fig. 18. SLJ tests: (a) specimen dimensions in mm, (b) force-displacement curves. Experiments “Exp”, mesoscopic model “Meso”, macroscopic model experimental calibration “Macro exp”, macroscopic model virtual calibration “Macro virt”.

5.2. Component test and simulation

This section presents a test setup for three-sheet SPR connections with a component based on a design proposed by Reil et al. [32]. The component was loaded under quasi-static conditions in a three-point bending setup, allowing for a subsequent failure of the SPR connections. Two 2 mm thick hat-profile sections were sandwiched together with a 1 mm flat sheet section in between and were joined with a row of eight SPR along the centerline. The stack of hat profiles and middle plate was identical to the investigated SPR connection in this work. The top hat-profile featured two 1 mm covering plates at both ends, whereas the bottom profile was covered along the entire length with a 1 mm covering plate as seen in Fig. 19. The covering plates were fastened with a row of M8 bolts which were used to prevent distortion of the cross-section of the profile during the test.

The dimensions of the component specimen are shown in Fig. 19a. The three-point bending test rig consisted of two lower posts and a punch with a 15 mm offset from the centerline. The offset ensured the asymmetric opening of the assembly and sequential rivet failure. The posts and the punch had a cylindrical shape with a radius of 25 mm.

The macroscopic model of the component test can be seen in Fig. 19c. The sheet metal parts were discretised with 2×2 mm under-integrated shell elements with five integration points through the thickness. The Belytschko-Tsay element formulation was applied together with a stiffness based hourglass control. The post and the punch were modelled using a rigid body formulation. A surface-to-surface contact formulation with a general friction coefficient of 0.15 was used between all contact pairs. The closing plates were tied to the hat profiles as no separation of the parts was observed in the tests. In addition, the M8 bolt heads were modelled using solid elements tied to the sheets. The eight connector pairings (upper and lower) were placed along the centerline. The work-hardening from the forming of the profiles was accounted for by including the resulting plastic strains. Mass scaling was applied to achieve a time-step of 3.3×10^{-4} ms with a total simulation time of 2000 ms. A 12%

mass increase of the deformable components was therefore considered reasonable.

The force-displacement curves from the experiments and the macroscopic simulations are given in Fig. 20a. The test was repeated four times and all specimens showed a similar gradual increase of force to approximately 8.7 kN and the same overall deformation mode. Sudden failure of the first rivet at the right outermost position dropped the force to approximately 6.5 kN. The force then increased slightly for all tests and reached a plateau which was followed by the rapid failure of the second rivet. Another force plateau was followed by the third rivet failure at approximately 4.8 kN, followed by a decrease to approximately 3.9 kN. The test was stopped at 65 mm with no failure of the remaining 5 rivets. All three rivets failed in rivet-pull-out mode, see Fig. 7. That means that the bottom 2 mm sheet separated from the stack while the 1 mm middle sheet stayed connected to the 2 mm top sheet via the rivet, as seen in Fig. 20d. Figure 20b shows the top hat profile buckling in the punch contact area but no signs of material fracture or cracks were observed.

The macroscopic models both with the experimentally and the virtually calibrated constraint models showed a good representation of the experimental behaviour. The initial stiffness was well captured by both models. The experimentally-calibrated macroscopic model is within the dispersion of the experimental curves. The virtually-calibrated macroscopic model gave an error of around 5 % for the peak force, and around 15 % for the displacements at failure. Both models showed the sequential failure of three bottom connectors, with the matching rivet-pull-out mode, as seen in Fig. 20e. Failure of the first rivet using the experimentally calibrated model was captured at the matching punch displacement but the second and third rivets failed slightly earlier than the rivets in the experiment. The virtually calibrated model showed earlier failure of the first rivet and failure of the second rivet close after. The third rivet failed also earlier accordingly. Buckling of the top hat profile was in good agreement with the experiments as seen in Fig. 20c.

The experimentally calibrated SPR models were able to give a satisfactory representation of the component behaviour. Also the virtually calibrated connector models gave a satisfactory response of the component model, promoting the use of virtual cross tests for calibration. Despite discrepancies in the cross test modelling where the virtual cross test showed higher strength especially under shear loading, the virtually fitted macroscopic model performed well. It should be noted that this form of component test enabled a tension-dominated loading of the rivets and therefore does not challenge the macroscopic models in the shear regime.

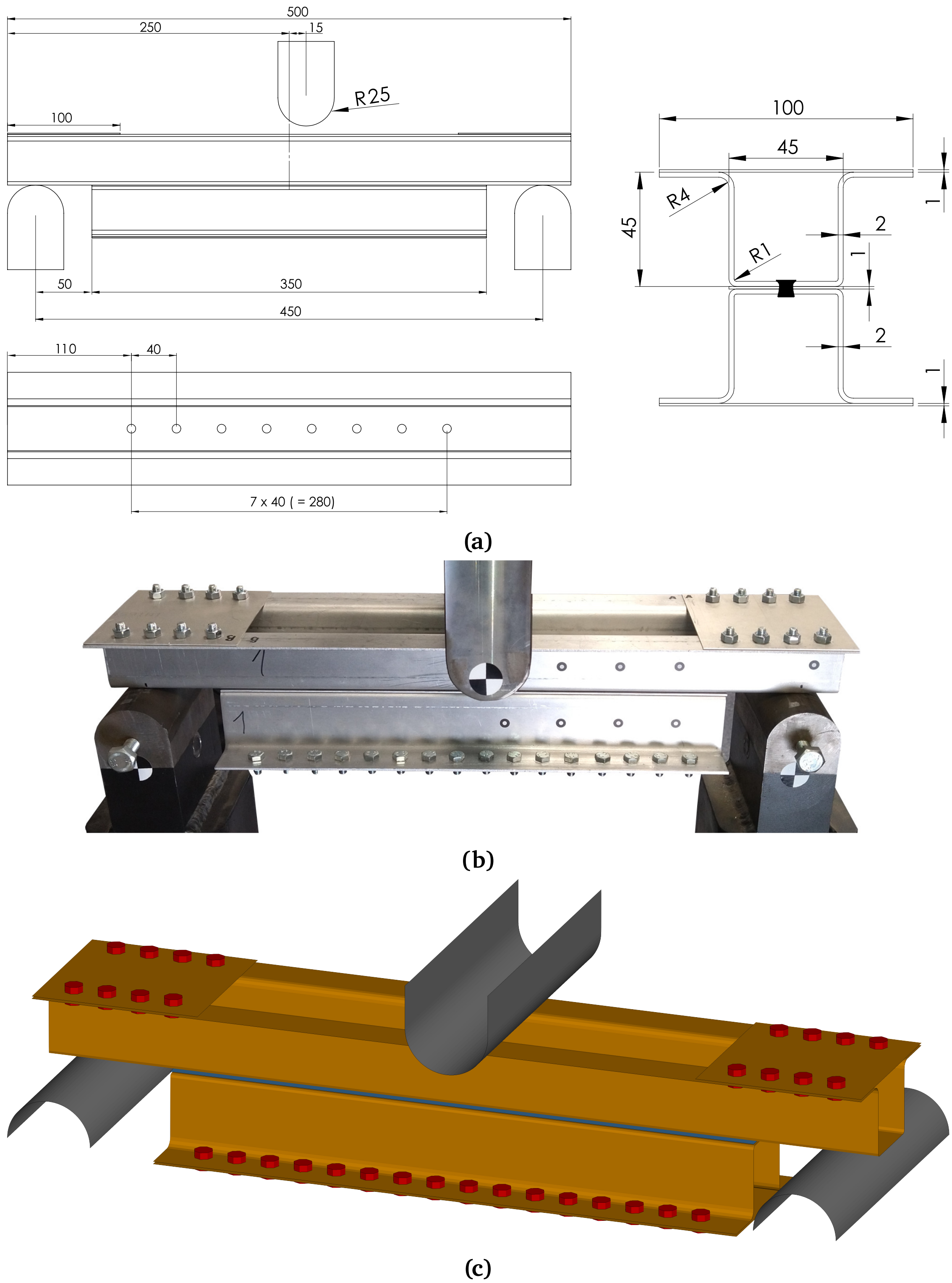

Fig. 19. Component test setup: (a) specimen dimensions in mm, (b) real test specimen and (c) macroscopic component test model.

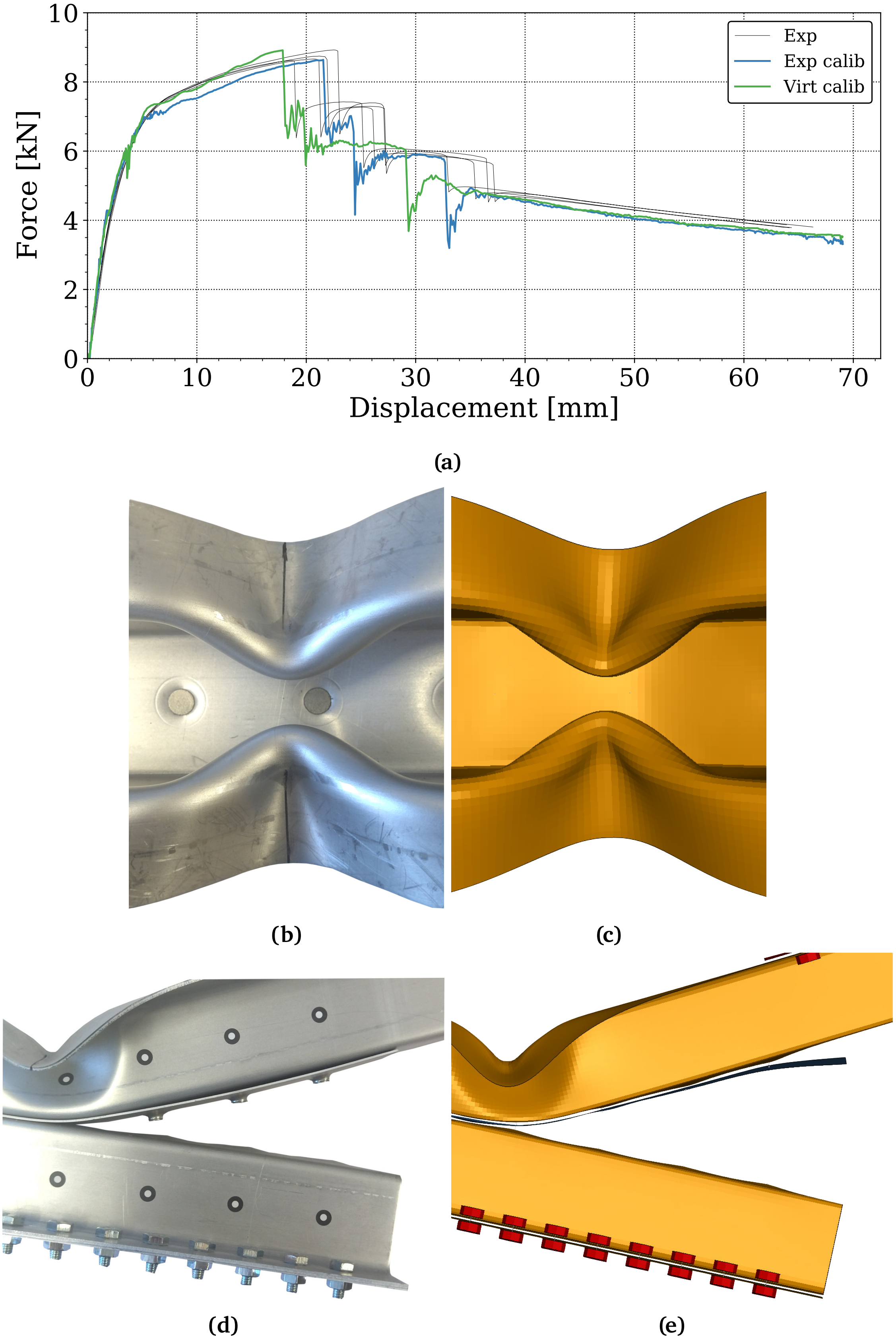

Fig. 20. Component test results: (a) force-displacement curve from experiments and simulations, (b, c) buckling below punch, (d, e) rivet failure. Experiments "Exp", macroscopic model experimental calibration "Exp calib", macroscopic model virtual calibration "Virt calib".

6. Conclusions

This work investigated a virtual calibration strategy for a three-sheet SPR connection model with aluminium sheets. In addition, validation methods at the joint unit level as well as the component level were presented. Different scales, from the riveting process and single joint unit to a component with multiple connections, were addressed while using both detailed mesoscopic and large-scale macroscopic modelling techniques. The performance of a virtually calibrated connector model was assessed. The following main conclusions are drawn:

- A state-of-the-art riveting process simulation was able to predict the geometry of a three-sheet SPR joint with the process parameters adjusted to approximate the physical geometry. Force measurements from the SPR machine should be used in addition for adjusting the process parameters.

- Cross tests were successfully replicated with detailed mesoscopic models, although deviations likely arose from discrepancies in the riveting process simulation. The mismatch could be due to the limitations of the model, as neither strain rate sensitivity nor temperature were accounted for.

- Despite the deviations seen in the virtual experiments, the macroscopic models calibrated with them nonetheless provided reasonable predictions of the experimental tests.

- The virtually calibrated connector models showed reliable behaviour when applied to the component test simulation, supporting the virtual calibration strategy presented. Slightly earlier connector failure was observed in the virtually calibrated model, which is explained by a lower failure displacement visible in the tensile and mixed mode cross tests.

- The virtual calibration process is based on a chain of simulations, where errors in the models can add up and lead to uncertainty in the final large-scale model. However, inaccuracies in the model may be offset by the decreased need for extensive physical testing.

7. Acknowledgements

The authors would like to acknowledge the financial support from the Centre for Advanced Structural Analysis, SFI-CASA (Project No. 237885), funded by the Research Council of Norway and NTNU.

References

[1] G. Meschut, V. Janzen, and T. Olfermann. Innovative and highly productive joining technologies for multi-material lightweight car body structures. *Journal of Materials Engineering and Performance*, 23(5):1515–1523, 2014.

[2] R. Haque. Quality of self-piercing riveting (SPR) joints from cross-sectional perspective: A review. *Archives of civil and mechanical engineering*, 18(1):83–93, 2018.

[3] D. Li, A. Chrysanthou, I. Patel, and G. Williams. Self-piercing riveting-a review. *The International Journal of Advanced Manufacturing Technology*, 92:1777–1824, 2017.

[4] K. Mori, Y. Abe, and T. Kato. Self-pierce riveting of multiple steel and aluminium alloy sheets. *Journal of Materials Processing Technology*, 214(10):2002–2008, 2014.

[5] A. H. Ibrahim and D. S. Cronin. Mechanical testing of adhesive, self-piercing rivet, and hybrid jointed aluminum under tension loading. *International Journal of Adhesion and Adhesives*, 113: 103066, 2022.

[6] X. Sun. Dynamic strength evaluation/crashworthiness of self-piercing riveted joints. In *Self-Piercing Riveting*, pages 56–78. 2014.

[7] Y. Fang, L. Huang, Z. Zhan, S. Huang, X. Liu, Q. Chen, H. Zhao, and W. Han. A framework for calibration of self-piercing riveting process simulation model. *Journal of Manufacturing Processes*, 76:223–235, 2022.

[8] F. Kappe, S. Wituschek, M. Bobbert, M. Lechner, and G. Meschut. Joining of multi-material structures using a versatile self-piercing riveting process. *Production Engineering*, 17(1):65–79, 2023.

[9] H. Zhao, L. Han, Y. Liu, and X. Liu. Analysis of joint formation mechanisms for self-piercing riveting (SPR) process with varying joining parameters. *Journal of Manufacturing Processes*, 73 (September 2021):668–685, 2022.

[10] F. Hirsch, S. Müller, M. Machens, R. Staschko, N. Fuchs, and M. Kästner. Simulation of self-piercing rivetting processes in fibre reinforced polymers: Material modelling and parameter identification. *Journal of Materials Processing Technology*, 241:164–177, 2017.

[11] F. Hönsch, J. Domitner, C. Sommitsch, and B. Götzinger. Modeling the Failure Behavior of Self-Piercing Riveting Joints of 6xxx Aluminum Alloy. *Journal of Materials Engineering and Performance*, 29(8):4888–4897, 2020. ISSN 15441024.

[12] M. A. Karim, T. E. Jeong, W. Noh, K. Y. Park, D. H. Kam, C. Kim, D. Nam, H. Jung, and Y. Park. Joint quality of self-piercing riveting (SPR) and mechanical behavior under the frictional effect of various rivet coatings. *Journal of Manufacturing Processes*, 58(August):466–477, 2020.

[13] L. Duan, Z. Du, H. Ma, W. Li, W. Xu, and X. Liu. Simplified modelling of self-piercing riveted joints and application in crashworthiness analysis for steel-aluminium hybrid beams. *Journal of Manufacturing Processes*, 85:948–962, 2023.

[14] N. Leconte, B. Bourel, F. Lauro, C. Badulescu, and E. Markiewicz. Strength and failure of an aluminum/PA66 self-piercing riveted assembly at low and moderate loading rates: Experiments and modeling. *International Journal of Impact Engineering*, 142(2020), 2020.

[15] C.-x. Wang, T. Suo, H.-m. Gao, and P. Xue. Determination of constitutive parameters for predicting dynamic behavior and failure of riveted joint: Testing, modeling and validation. *International Journal of Impact Engineering*, 132(November 2018), 2019.

[16] D. Wang, D. Kong, C. Xie, S. Li, and L. Zong. Study on the effect of rivet die parameters on joint quality of self-piercing riveting employed 3D modeling and MCDM method. *International Journal of Advanced Manufacturing Technology*, 119(11-12):8227–8241, 2022.

[17] Aman Rusia and Stefan Weihe. Development of an end-to-end simulation process chain for prediction of self-piercing riveting joint geometry and strength. *Journal of Manufacturing Processes*, 57(July):519–532, 2020.

[18] V. André, M. Costas, M. Langseth, and D. Morin. Behavior and large-scale modeling of multi-sheet aluminum connections with self-piercing rivets. *Journal of Manufacturing Science and Engineering*, 145(10), 2023.

[19] User manual - eCorr - Digital Image Correlation Tool. *https://folk.ntnu.no/egilf/ecorr/doc/*. NTNU, Trondheim, Norway, 2017.

[20] R. Khezri, E. Sjöström, and A. Melander. Self-piercing riveting of high strength steel. *Swedish Institute for Metal Research*, IM-2000-55, 2000.

[21] R. Porcaro, A. Hanssen, M. Langseth, and A. Aalberg. Self-piercing riveting process: An experimental and numerical investigation. *Journal of Materials Processing Technology*, 171:10–20, 2006.

[22] Samuel Baha II. Numerical investigation of the rivet installation in an adhesively bonded joint and the load transfer in a bolted/bonded hybrid joint. *SAE International Journal of Materials and Manufacturing*, 8(1):45–55, 11 2014.

[23] F. D. Hönsch, J. Domitner, and C. Sommitsch. Deformation behavior of high-strength steel rivets for self-piercing riveting applications. *AIP Conference Proceedings*, 2113(1), 2019.

[24] LS-DYNA Keyword User's Manual Volume I version 11. *https://www.dynasupport.com/manuals/ls-dyna-manuals/ls-dyna-manuals*. Livermore, California, 2019.

[25] P. O. Bouchard, T. Laurent, and L. Tollier. Numerical modeling of self-pierce riveting - From riveting process modeling down to structural analysis. *Journal of Materials Processing Technology*, 202:290–300, 2008.

[26] N. Karathanasopoulos, K. S. Pandya, and D. Mohr. Self-piercing riveting process: Prediction of joint characteristics through finite element and neural network modeling. *Journal of Advanced Joining Processes*, 3:100040, 6 2021.

[27] J. F.C. Moraes, J. B. Jordon, and E. I. Ilieva. Influence of the Friction Coefficient in Self-Pierce Riveting Simulations: A Statistical Analysis. *SAE International Journal of Materials and Manufacturing*, 11(2):123–130, 2018.

[28] Li Huang, John V. Lasecki, Haiding Guo, and Xuming Su. Finite Element Modeling of Dissimilar Metal Self-piercing Riveting Process. *SAE International Journal of Materials and Manufacturing*, 7(3):2014–01, 4 2014.

[29] A. Hershey. The plasticity of an isotropic aggregate of anisotropic face-centered cubic crystals. *Journal of Applied Mechanics-Transactions of the ASME*, pages 241–249, 1954.

[30] M. Costas, D. Morin, O. S. Hopperstad, T. Børvik, and M. Langseth. A through-thickness damage regularisation scheme for shell elements subjected to severe bending and membrane deformations. *Journal of the Mechanics and Physics of Solids*, 123:190–206, 2019.

[31] A. G. Hanssen, L. Olovsson, R. Porcaro, and M. Langseth. A large-scale finite element point-connector model for self-piercing rivet connections. *European Journal of Mechanics, A/Solids*, 29 (4):484–495, 2010.

[32] M. Reil, D. Morin, M. Langseth, and O. Knoll. A novel tests set-up for validation of connector models subjected to static and impact loadings. *International Journal of Impact Engineering*, 158: 103978, 2021.

[33] J. K. Sønstabø, D. Morin, and M. Langseth. Testing and modelling of flow-drill screw connections under quasi-static loadings. *Journal of Materials Processing Technology*, 255:724–738, 2018.

Appendix A. Material modelling

An isotropic plasticity model was used for modelling of the sheet and the rivet material. The yield function can be written as

$$f = \sigma_{\text{eq}} - (\sigma_0 + R) \leq 0, \tag{A.1}$$

where σ_{eq} is the equivalent stress, σ_0 the initial yield stress and R is the isotropic hardening variable. For the constitutive modelling in the mesoscopic models, the von Mises equivalent stress was used, described as:

$$\sigma_{\text{eq,vM}} = \left[\frac{1}{2}\left(|\sigma_1 - \sigma_2|^2 + |\sigma_2 - \sigma_3|^2 + |\sigma_3 - \sigma_1|^2\right)\right]^{\frac{1}{2}}, \tag{A.2}$$

where the principal stresses are denoted by σ_1, σ_2 and σ_3. For the macroscopic models, the Hershey-Hosford [29] equivalent stress formulation was applied, which is a generalised form of the von Mises equivalent stress equation, denoted as:

$$\sigma_{\text{eq,H}} = \left[\frac{1}{2}\left(|\sigma_1 - \sigma_2|^m + |\sigma_2 - \sigma_3|^m + |\sigma_3 - \sigma_1|^m\right)\right]^{\frac{1}{m}}, \tag{A.3}$$

where $m = 8$ is a material dependent exponent. For both the mesoscopic and the macroscopic models, the isotropic hardening of the aluminium was realised by a three-term Voce hardening rule, described as:

$$R = \sum_{i=1}^{N} Q_{\text{R}i}\left(1 - \exp\left(-\frac{\theta_{\text{R}i}}{Q_{\text{R}i}}p\right)\right), \tag{A.4}$$

where N is the number of terms used. $Q_{\text{R}i}$ are the final stress values where hardening saturates and $\theta_{\text{R}i}$ are the initial hardening moduli. The term is indicated with i and the equivalent plastic strain is denoted p. The material parameters for the aluminium sheets were taken from [18] et al. The isotropic hardening of the rivet material was realised by a combination of power-law and Voce hardening, resulting in a stronger work-hardening at initial yielding and a linear work-hardening modulus for higher strains, described by:

$$R = (Q + Hp) \cdot (1 - \exp(-cp)), \tag{A.5}$$

where Q changes the onset of linear hardening, H is the linear work hardening modulus, c is the initial strain hardening gradient and p denotes the equivalent plastic strain. The Hershey-Hosford yield criterion was not available for the mesoscopic modelling (*MAT_PIECEWISE_LINEAR_PLASTICITY in LS-Dyna) and the von Mises yield criterion had to be used instead.

Appendix B. Constraint model

The constraint model by Hansen et al. [31] defines a master and a slave sheet, represented by master and slave node regions. The spatial relative deformation is decomposed into a normal and tangential part, where the normal direction is orthogonal to the sheets' mid-surface and the tangential direction is in-plane of the sheets.

The relative nodal displacements between the sheets, also called stretches, are denoted δ_{n} (normal) and δ_{t} (tangential) stretch, respectively. The model calculates a normal f_{n} and a tangential component f_{t} from these stretch variables. The governing equations for calculation of the forces components are given in Table B.5. The model calculates a damage variable named maximum effective displacement η_{max}. The damage evolves during joint deformation and depends on the loading mode. The damage variable indicates maximum joint opening and drives joint deletion. Nine parameters are needed for model calibration which are found by inverse engineering of experimental tests in different loading directions. The moment acting on the master and slave sheets is based on the force components and the sheet thicknesses. The models allow for free rotation around the fastener axis, since connections like SPR show neglectable twisting resistance.

Table B.5. Constraint model, governing equations [31, 33].

Total stretch $\boldsymbol{\delta}$ defined as the vector between slave end and original location on the deformed slave sheet. Normal and tangential stretch: $\boldsymbol{\delta} = \boldsymbol{\delta}_{\mathrm{n}} + \boldsymbol{\delta}_{\mathrm{t}}, \quad \delta_{\mathrm{n}} = \lvert \boldsymbol{\delta} \cdot \hat{\boldsymbol{n}}_{\mathrm{m}} \rvert,$ $\delta_{\mathrm{t}} = \lvert \boldsymbol{\delta} \cdot \hat{\boldsymbol{n}}_{\mathrm{t}} \rvert, \quad \hat{\boldsymbol{n}}_{\mathrm{t}} = \hat{\boldsymbol{n}}_0 \times \hat{\boldsymbol{n}}_{\mathrm{m}}$	Loading direction: $\theta = \arctan\left(\frac{\delta_{\mathrm{t}}}{\delta_{\mathrm{n}}}\right)$
Forces are calculated directly from mathematical expressions: $f_{\mathrm{n}} = \frac{f_{\mathrm{n}}^{\max}\delta_{\mathrm{n}}}{\eta_{\max}\delta_{\mathrm{n}}^{\mathrm{fail}}}\hat{f}_{\mathrm{n}}, \quad f_{\mathrm{t}} = \frac{f_{\mathrm{t}}^{\max}\delta_{\mathrm{t}}}{\eta_{\max}\delta_{\mathrm{t}}^{\mathrm{fail}}}\hat{f}_{\mathrm{t}},$ where $\hat{f}_{\mathrm{n}} = \begin{cases} 1 - \left(\frac{\xi_{\mathrm{n}} - \eta_{\max}}{\xi_{\mathrm{n}}}\right)^8, & \eta_{\max} \leq \xi_{\mathrm{n}} \\ 1 - \frac{\eta_{\max} - \xi_{\mathrm{n}}}{1 - \xi_{\mathrm{n}}}, & \eta_{\max} > \xi_{\mathrm{n}} \end{cases}$ $\hat{f}_{\mathrm{t}} = \begin{cases} 1 - \left(\frac{\xi_{\mathrm{t}} - \eta_{\max}}{\xi_{\mathrm{t}}}\right)^8, & \eta_{\max} \leq \xi_{\mathrm{t}} \\ 1 - \frac{\eta_{\max} - \xi_{\mathrm{t}}}{1 - \xi_{\mathrm{t}}}, & \eta_{\max} > \xi_{\mathrm{t}} \end{cases}$ Exponent of 8 suggested by Hanssen et al. [31] but can be changed in the LS-DYNA solvers.	Damage variables: $\eta = \left[\xi + \frac{1-\xi}{\alpha}\sqrt{\left(\frac{\delta_{\mathrm{n}}}{\delta_{\mathrm{n}}^{\mathrm{fail}}}\right)^2 + \left(\frac{\delta_{\mathrm{t}}}{\delta_{\mathrm{t}}^{\mathrm{fail}}}\right)^2}\right]$ $\xi = 1 - \frac{27}{4}\left(\frac{2\theta}{\pi}\right)^2 + \frac{27}{4}\left(\frac{2\theta}{\pi}\right)^3$ $\alpha = \begin{cases} \frac{\xi_{\mathrm{t}} - \eta_{\max}}{\eta_{\mathrm{t}}}\alpha_1 + \frac{\eta_{\max}}{\eta_{\mathrm{t}}}\alpha_2, & \eta_{\max} < \xi_{\mathrm{t}} \\ \frac{1 - \eta_{\max}}{1 - \xi_{\mathrm{t}}}\alpha_2 + \frac{\eta_{\max} - \xi_{\mathrm{t}}}{1 - \xi_{\mathrm{t}}}\alpha_3, & \eta_{\max} \geq \xi_{\mathrm{t}} \end{cases}$